Structure and Charge Regulation Strategy Enabling Superior Cyclability for Ni-Rich Layered Cathode Materials

Wei Huang, Wenjin Li, Lve Wang, He Zhu, Min Gao, Huan Zhao, Jinling Zhao, Xueling Shen, Xiaodan Wang, Ze Wang, Chuanlei Qi, Wei Xiao, Lei Yao, Jiantao Wang,* Weidong Zhuang,* and Xueliang Sun*

Ni-rich layered oxides are significantly promising cathode materials for commercial high-energy-density lithium-ion batteries. However, their major bottlenecks limiting their widespread applications are capacity fading and safety concerns caused by their inherently unstable crystal structure and highly reactive surface. Herein, surface structure and bulk charge regulation are concurrently achieved by introducing high-valence Ta^{5+} ions in Ni-rich cathodes, which exhibit superior electrochemical properties and thermal stability, especially a remarkable cyclic stability with a capacity retention of 80% for up to 768 cycles at a 1C rate versus Li/Li^+. Due to the partial Ta enrichment on surface, the regulated surface enables high reversibility of Li^+ insertion/extraction by preventing surface Ni reduction in deep charging. Moreover, bulk charge regulation that boosts charge density and its localization on oxygen remarkably suppresses microcracks and oxygen loss, which in turn prevents the fragmentation of the regulated surface and structural degradation associated with oxygen skeleton. This study highlights the significance of an integrated optimization strategy for Ni-rich cathodes and, as a case study, provides a novel and deep insights into the underlying mechanisms of high-valence ions substitution of Ni-rich layered cathodes.

1. Introduction

The increasing worldwide demand for high-energy-density lithium-ion batteries has proposed new challenges to high capacity, strong cyclic stability, and safe cathode materials.[1] Owing to their high specific capacities and low costs, Ni-rich layered oxides ($LiNi_xCo_yAl_{1-x-y}O_2$ and $LiNi_xCo_yMn_{1-x-y}O_2$, $0.8 \leq x \leq 1$) are considered as the most promising cathode materials for commercial applications.[2] However, their severe structural and thermal instabilities induce capacity fading and safety issues, hindering their widespread commercialization.[3]

Among the most significant challenges are the surface chemical and structural instabilities of such layered oxides. Owing to the existence of highly active Ni^{4+} in deep delithiation, the surface regions of the Ni-rich cathodes exhibit high reactivity and instability;[4] thus, they can easily undergo undesirable side reactions

W. Huang, L. Wang, M. Gao, H. Zhao, J. Zhao, X. Shen, X. Wang, Z. Wang, C. Qi, W. Xiao, J. Wang
National Power Battery Innovation Center
Grinm Group Corporation Limited
Beijing 100088, China
E-mail: wangjt@glabat.com

W. Huang, W. Zhuang
School of Metallurgical and Ecological Engineering
University of Science and Technology Beijing
Beijing 100083, China
E-mail: wdzhuang@ustb.edu.cn

W. Huang, L. Wang, M. Gao, J. Zhao, X. Shen, X. Wang, Z. Wang, C. Qi, J. Wang
China Automotive Battery Research Institute Co. Ltd
Beijing 101407, China

W. Huang, J. Wang, W. Zhuang
General Research Institute for Nonferrous Metals
Beijing 100088, China

W. Li, L. Yao
College of Materials Science and Engineering
Shenzhen University
Shenzhen 518060, China

H. Zhu
Department of Physics
City University of Hong Kong
Hong Kong 999077, China

W. Zhuang
Beijing Key Laboratory of Green Recovery and Extraction
of Rare and Precious Metals
University of Science and Technology Beijing
Beijing 100083, China

X. Sun
Department of Mechanical and Materials Engineering
University of Western Ontario
London, Ontario N6A 5B9, Canada
E-mail: xsun9@uwo.ca

with electrolytes and irreversible structural deterioration through continuous cation migration into Li layers, leading to rapid capacity fading.[5] To address these problems, numerous researchers have devised various coating strategies aimed at prohibiting direct contact between cathodes and electrolytes.[6] Despite various degrees of success, most of these strategies have produced limited structural stabilization effects. One promising approach for optimizing the surface structure of the Ni-rich cathodes involves designing a surface doping layer with Ti segregation, which exhibits a stable cathode–electrolyte interface.[7] However, the lack of cooperation from bulk structural stability and integrity leads to limited promotion of electrochemical properties. For example, inter/intragranular cracks arising from anisotropic lattice shrinkage expose fresh surface to electrolytes for side reactions upon cycling; their propagation induces the formation of isolated coating islands and accelerates failure of the surface modification strategy.[8] By introducing alkali metal ions (e.g., Na$^+$) in the Li layer that produces screen effect, severe c-axis lattice shrinkage of Ni-rich cathodes was suppressed, which prevented the microcracks and increased the cyclic stability.[9] Another attractive strategy showed that a morphology-controlled Ni-rich cathode, with rod-shaped primary particles growing in the radial direction, relieved the internal lattice strain, thereby improving the particle integrity and cyclic stability.[10] However, high concentration of foreign ions in the Li layer lowers the battery capacity and the complicated synthetic control introduces practical challenges. Thus, suitable methods for integrating the surface and bulk structures for fine material design are highly desirable for Ni-rich cathode materials to overcome their intrinsic drawbacks.

Moreover, oxygen loss in deep delithiation is a significant source of structural instability, which decreases migration energy barrier and triggers continuous cation migration, thus accelerating structural collapse.[11] The surface released oxygen can oxidize electrolyte solvents and subsequently generate heat and by-products, resulting in serious safety risks.[12] Generally, the lithiation/delithiation process in conventional layered cathodes, such as Ni-rich oxides, LiCoO$_2$, are considered as accompanied by the transition metal (TM; such as Ni and Co) redox with oxygen (O) as a bystander, due to the relatively constant pinning of the TM redox couples (Ni$^{2+/3+/4+}$, Co$^{3+/4+}$) at top of the O 2p band.[13] However, with increasing evidence of O$_2$ release in Ni-rich cathodes during cycling, the possible mechanisms associated with irreversible charge compensation and/or oxidation of lattice O have been widely investigated.[14] Yet, understanding the origin of oxygen loss remains ambiguous. Therefore, an in-depth exploration of the oxygen loss mechanisms and practical solutions, with a clarification of evolutionary path of oxygen charge, is required to provide a rational guideline for designing a more stable and safe cathode.

In this study, surface structure and bulk charge were regulated concurrently by introducing high-valence Ta^{5+} ions in Ni-rich LiNi$_{0.88}$Co$_{0.10}$Al$_{0.02}$O$_2$ cathodes to stabilize both bulk and surface structures, achieving remarkable cycling performance and thermal stability.

By incorporating first-principles calculations and combined characterization, including spherical aberration-corrected transmission electron microscopy (AC-TEM), synchrotron X-ray absorption spectroscopy (XAS), differential electrochemical mass spectrometry (DEMS), as well as various in situ coupling techniques, an integrated perspective of the functional mechanisms of high-valence Ta^{5+} ion substitution in Ni-rich cathodes was presented. We reveal that the critical role of the Ta-rich regulated surface structure is to prevent Ni reduction and migration in deep charging, thereby enabling high Li$^+$ insertion/extraction reversibility and better cyclability. Furthermore, oxygen charge excess and localization induced by Ta substitution resists the delocalized nature of oxygen charge in layered cathodes upon delithiation. This finding is the fundamental reason for the suppressed microcracks and oxygen loss, presenting improved structural stability and integrity, which in turn prevents the fragmentation of the regulated surface after long-term cycling. Meanwhile, as a case study, we clarify previously unidentified connections among the electrochemical behaviors, crystal structures, and electronic structures after introducing high-valence ions.

2. Results and Discussion

2.1. Surface Chemical and Structural Characterization

As model materials, LiNi$_{0.88}$Co$_{0.10}$Al$_{0.02}$Ta$_{0.004}$O$_2$ (NCAT1) and LiNi$_{0.88}$Co$_{0.10}$Al$_{0.02}$Ta$_{0.008}$O$_2$ (NCAT2) were synthesized using a simple pre-coating and sintering method, as described in the experimental section (the Ta concentrations were optimized). Pristine LiNi$_{0.88}$Co$_{0.10}$Al$_{0.02}$O$_2$ (NCA) was prepared under the same sintering conditions. The precise component concentrations were confirmed by inductively coupled plasma (ICP) results (Table S1, Supporting Information). As discussed below, Ta exhibits a spontaneous surface enrichment and significantly affects the surface chemical and structural properties.

Specifically, the X-ray diffraction (XRD) patterns of both samples (Figure S1, Supporting Information) display a well-ordered $R\bar{3}m$ structure without impurity phases. The lower (003) peaks of NCAT1 and NCAT2 compared with that of NCA demonstrate that the Ta ions doped in the lattice increases the lattice parameters. This result is verified by the lattice parameter values calculated by Rietveld refinement method (Figure S2 and Tables S2–S4, Supporting Information). In addition, NCAT1 shows smooth and clear surface that is similar to that of NCA (Figure S3, Supporting Information). Notably, the X-ray photoelectron spectroscopy (XPS) depth profiles of NCAT1 (**Figure 1**a) show that the intensities of the Ta 4f peaks gradually decrease with an increase in the etching time. The derived Ta atomic percent concentration confirms that a partial enrichment of Ta on surface. Besides, both STEM-EDS and EPMA-WDS cross-sectional line scan profiles (Figures S4 and S5, Supporting Information) indicate that the Ta-element concentration on the particle surface is higher than that in the center of the particle of NCAT1, which also illustrates a partial Ta enrichment on surface. This phenomenon can be attributed to the limited doping kinetics under the optimal lithiation temperature (730 °C), as also reported previously.[15] The specific synthesis method employed in this study is pre-coating followed by sintering, allowing for enlarged diffusion paths for dopants, which potentially results in dopants enrichment on the surface and

ADVANCED
SCIENCE NEWS

www.advancedsciencenews.com

NANO · MICRO

small

www.small-journal.com
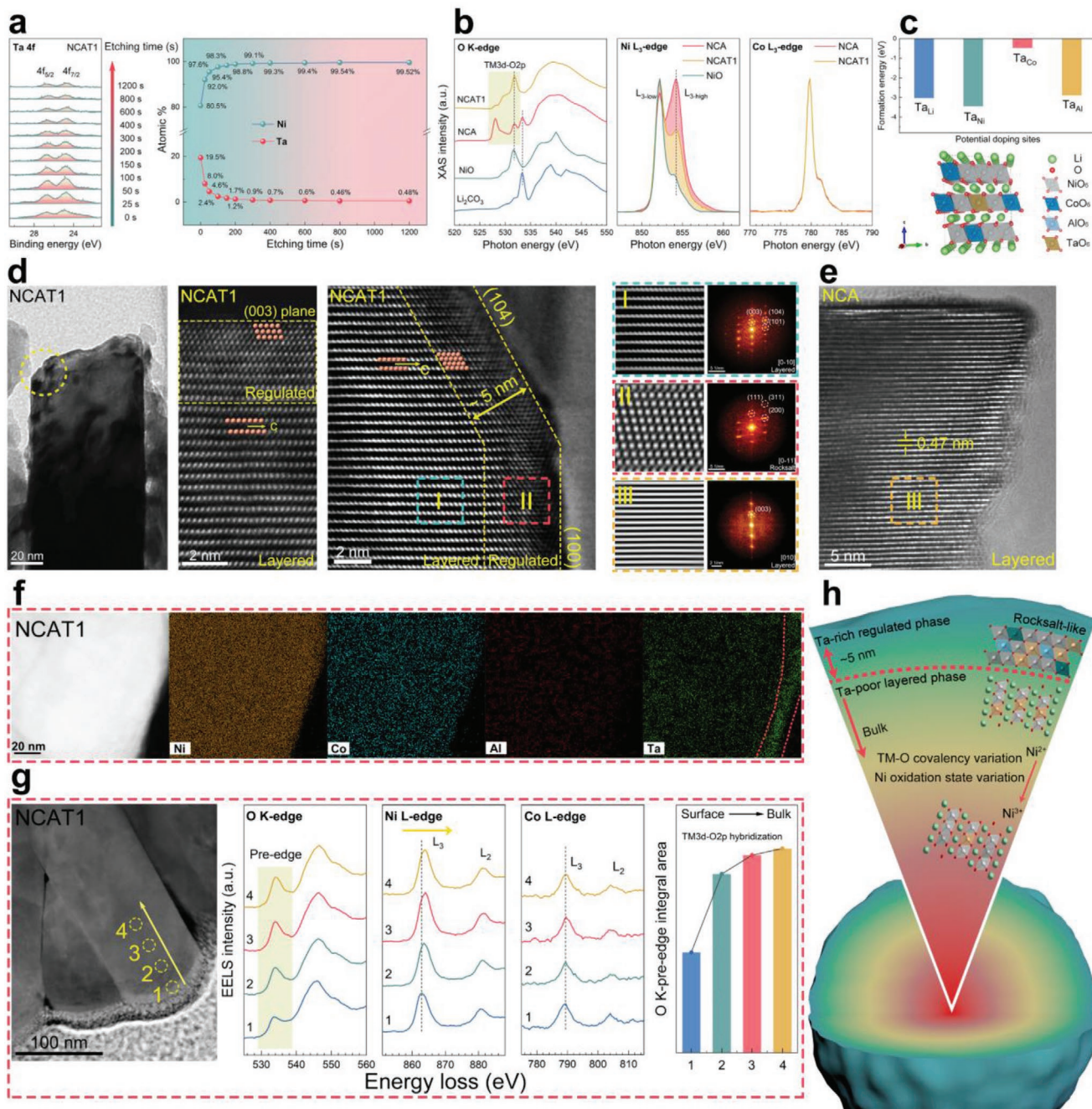
Figure 1. Surface chemical and structural characterization: a) XPS depth profiles of Ta 4f peaks of NCAT1 with increasing etching time and the corresponding Ni/Ta atomic ratio for each depth profile; b) Normalized O K-edge, Ni L_3-edge, and Co L_3-edge XAS spectra of NCA and NCAT1 in TEY mode; c) Formation energies of Ta substituting potential sites (Ni, Co, Al, and Li) and NCAT supercell ($Li_{48}Ni_{41}Co_5Al_1Ta_1O_{96}$); d) the bright-field TEM image and the HADDF images near the surface of NCAT1; the intensified images and the FFT maps from the selected green, red, and yellow region, respectively; e) the HRTEM image of NCA; f) the STEM-EDS mappings of Ni, Co, Al, and Ta elements of NCAT1; g) the EELS spectra of the O K-edge, Ni L-edges, and Co L-edges recorded in the selected regions in the STEM image and the O K-pre-edge normalized integrated peak areas of the marked regions; h) schematic illustration of the surface structural regulation and the Ta element distribution.

an optimal doping concentration in the bulk. Accordingly, this strategy is expected to strengthen the surface and bulk structures simultaneously.

Furthermore, the synchrotron XAS spectra of the O K-edge, Ni L_3-edge, and Co L_3-edge in total electron yield (TEY) mode provide complementary insights into the effects of Ta doping

on the surface, as shown in Figure 1b. The XAS measurement with a surface-sensitive TEY mode primarily obtains information regarding the particle surface, with a probing depth of ≈10 nm. The XAS spectra of NiO and Li_2CO_3 were also acquired for reference. The most significant differences are in the pre-edge regions of the O K-edge spectra. The main pre-edge peak

of NCA at ≈528 eV corresponds to electron transitions from the O 1s level to the Ni^{3+} 3d–O 2p hybridized level, demonstrating that the Ni oxidation state of NCA is 3+. By contrast, the peak shifts to a higher energy of ≈532 eV in NCAT1, which reflects the Ni^{2+} 3d–O 2p hybridized level, confirming that the formal oxidation state of Ni is reduced from 3+ to nearly 2+ because of the enrichment of high-valence Ta^{5+} ions on the surface. The $Ni\ L_{3-low}/L_{3-high}$ ratio is used to evaluate the Ni oxidation states in a positive relationship.[16] The sharp decrease of the Ni L_{3-high} peak intensity (≈854 eV) also demonstrates that the Ni oxidation state of NCAT1 is lower than that of NCA. Otherwise, as shown in Figure S6 (Supporting Information), the XPS Ni 2p profiles indicate that the relative content of Ni^{2+} on the surface gradually increases with increasing Ta concentration. These results could be attributed to the substitution of high-valence Ta^{5+} for Ni^{3+} that provides local extra electrons, reducing the neighboring Ni oxidation state from 3+ to 2+. The Co L_3-edge spectrum of NCAT1 is similar to that of NCA, which shows that Ta does not affect the coordination environment of Co ions. Hence, Ta is expected to occupy Ni sites. By conducting first-principles calculations, the preferred substitution sites of Ta were evaluated. A 192-atom hexagonal NCA supercell ($Li_{48}Ni_{42}Co_5Al_1O_{96}$) was used for the calculations. The doping formation energy results (see the experimental section for calculation details) suggest that Ta doping at Ni sites is more energetically favorable than that at other sites (Figure 1c), which is consistent with the above described experiments.

Given the significant effect of Ta doping on the surface structure, further studies involving atomic-scale structural observations were conducted by performing spherical aberration-corrected scanning transmission electron microscopy (AC-STEM). As shown in Figure 1d,e, compared to NCA with a typical $R\bar{3}m$ layered structure, the high-angle annular dark-field (HAADF) images of NCAT1 show distinct regulated surface structures on the (003), (104), and (100) facets (rock-salt-like phase, $Fm\bar{3}m$ space group, ≈5 nm thickness), which are identified in the corresponding intensified images and the fast Fourier transformation (FFT) patterns. The regulated surface is expected to be stable owing to its high structural stability and lower electrochemical activity.[17] Furthermore, the energy-dispersive X-ray spectroscopy (EDS) mapping of Ta (Figure 1f) clearly shows that strong Ta signals are recorded on the surface compared with the bulk for NCAT1, suggesting that partial Ta enrichment induces surface structure regulation. As spatially resolved electron energy loss spectroscopy (EELS) can provide information regarding unoccupied states, similar to ensemble-averaged XAS measurements, as well as direct visualizations to probe the electronic structures in different regions, the crystal and electronic structures were effectively correlated by combining the XAS and EELS measurements. As shown in Figure 1g, the O K-edge EELS spectra show that the pre-edge integral intensity gradually decreases from the bulk to the surface, as confirmed by the histogram of the corresponding pre-edge integrated peak areas. Figure 1c also shows a remarkably reduced pre-edge peak integral intensity of NCAT1 compared to that of NCA in the O K-edge XAS spectra because of the Ta enrichment. Note that the pre-edge peaks integral intensity in the O K-edge spectra is mainly attributed to the TM–O hybridization degree in the TMO_6 crystal field, that is, the TM–O

covalency.[18] Stronger covalency introduces a larger population of O 2p electrons in the molecular antibonding orbitals, resulting in more intense pre-edge peaks. Hence, these results demonstrate that Ta substitution reduces the TM–O covalency (i.e., more ionic features in TM–O covalent bonds) and Ta concentration gradually decreases from the surface to the bulk in NCAT1, thus leading to the TM–O covalency variations. Moreover, the Ni L-edge EELS spectra show that the L_3-edge position gradually shifts toward higher energies as the recorded region moves inward, which suggests that the Ni oxidation state increases from the surface to the bulk. In the Co L-edges EELS spectra, the peak positions are barely changed, demonstrating that Ta introduced into the lattice mainly affects Ni, rather than Co. Al would not be affected by Ta substitution because of the intrinsic stable electronic configuration of Al^{3+} ions (Al^{3+}: $2s^22p^6$), which are not likely to gain or lose electrons.[19]

Overall, we obtained an integrated picture of the Ta distribution and surface structural changes induced by Ta substitution, as shown in Figure 1h. A regulated surface structure (rock-salt-like phase with a thickness of ≈5 nm) is constructed by the partial Ta enrichment on surface. In addition, the Ta doping concentration variation that decreases from the surface to the bulk of particles also results in the spatial variation of the Ni oxidation states and the TM–O covalency, the effects of which are discussed in detail in the following analyses. The Ta-rich regulated structure is expected to improve the surface structural and chemical stability and ultimately to improve the cyclic performance.

2.2. Electrochemical Performance

Thus far, this study focuses on how the Ta substitution affects the surface and bulk structures of NCA. This section elucidates the effects of Ta substitution on the electrochemical properties of both half-cells and full-cells, as presented in **Figure 2**, Figure S7, and Tables S5–S7 (Supporting Information) (detailed electrochemical data). Compared with NCA, NCAT1, and NCAT2 exhibit enhanced rate capabilities and cycling stabilities, despite the harsher conditions.

First, under the conventional testing condition (2.5–4.3 V, 25 °C), all the samples have similar discharge capacities (210.7, 213.3, and 207.9 mAh g^{-1} for NCA, NCAT1, and NCAT2, respectively, 1C = 200 mAh g^{-1}). However, NCAT1 and NCAT2 have higher initial Coulombic efficiencies than NCA (91% for NCAT1, 91.9% for NCAT2, and 89.9% for NCA (Table S5, Supporting Information)) and they exhibit higher rate capacities than NCA (Figure S7, Supporting Information), indicating that NCAT1 and NCAT2 can provide higher reversible capacities and stable structures to meet quick Li^+ insertion/extraction. Most importantly, NCAT1 and NCAT2 exhibit remarkable cycling stabilities at 1C (Figure 2d). The numbers of cycles corresponding to 80% capacity retention are 624 and 768 for NCAT1 and NCAT2, respectively, whereas that for NCA is only 162. In addition, NCAT1 and NCAT2 also provide high initial discharge capacities of up to 191.3 and 183.1 mAh g^{-1} for 1C cycling, respectively (186.7 mAh g^{-1} for NCA), which indicates that NCAT1 and NCAT2 can achieve high discharge capacities and superior cyclic performances simultaneously. Note that,
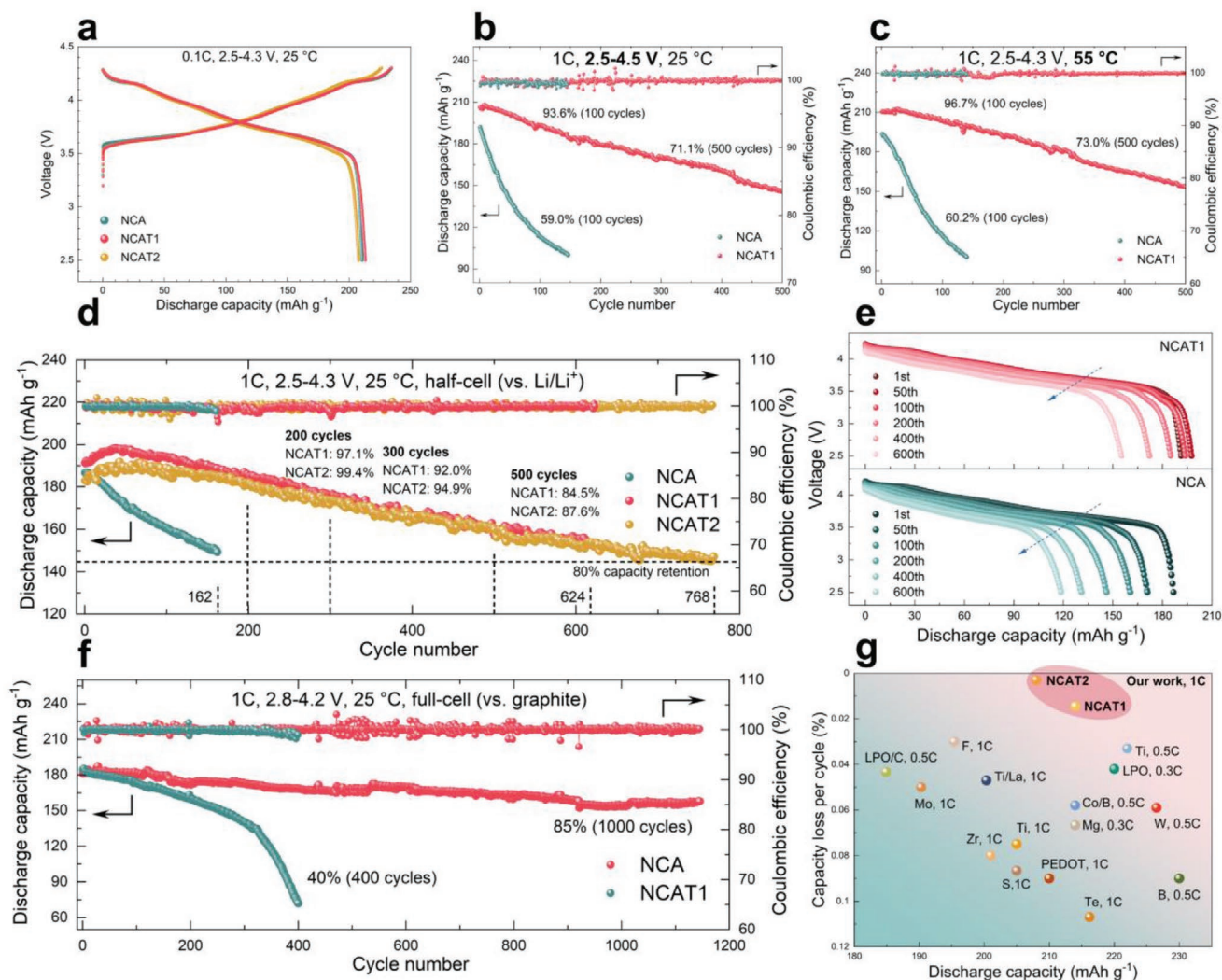
Figure 2. Electrochemical performances: a) First charge-discharge curves of NCA, NCAT1, and NCAT2 between 2.5–4.3 V versus Li/Li$^+$ at 25 °C; b) 1C cycling performance of NCA and NCAT1 with a cut-off voltage of 4.5 V; c) 1C cycling performance of NCA and NCAT1 at 55 °C; d, e) 1C cycling performance of NCA, NCAT1, and NCAT2 between 2.5–4.3 V versus Li/Li$^+$ at 25 °C and the corresponding discharge curves for the 1st, 50th, 100th, 200th, 400th, 600th cycles; f) Long-term 1C cycling tests in full cells of NCA and NCAT1 between 2.8–4.2 V versus graphite at 25 °C; g) Comparisons of the 0.1C discharge capacity and capacity loss per cycle for 200 cycles between our work and other modification strategies for Ni-rich cathodes reported recently.

in similar cases of initial cyclic capacity, the capacity retention of NCAT1 and NCAT2, to the best of our knowledge, are the best cycling performances ever reported for half-cell testing. In addition, the Coulombic efficiencies of NCA and NCAT1 are all relatively stable during cycling, even though testing temperature changes can lead to the Coulombic efficiency fluctuations to some extent. Figure 2e presents the discharge profiles at selected cycle numbers. It is apparent that NCA undergoes a marked voltage drop, whereas NCAT1 has more steady voltage curves, demonstrating that severe structural degradation is suppressed. Further, to highlight the improved performance of NCAT1, cycling tests with a charging cut-off voltage of 4.5 V and an elevated temperature of 55 °C were conducted, as displayed in Figure 2b,c. Evidently, NCAT1 exhibits a greater cycling stability than NCA despite the harsher conditions. To evaluate the feasibility of large-scale applications, long-term cycle-life tests of NCA and NCAT1 cathodes were performed in pouch-type

full cells (≈2 Ah) between 2.8 and 4.2 V at 1C versus graphite (equivalent to 4.3 V vs Li/Li$^+$). As shown in Figure 2f, NCA exhibits rapid capacity fading with a 40% capacity retention after 400 cycles, whereas NCAT1 exhibits a capacity retention of 85% after 1000 cycles, confirming the superior cycling stability for the full-cell application of NCAT1. Moreover, Figure 2g displays a crosswise comparison of the electrochemical performances among our work and previous studies, which further exhibits the outstanding comprehensive electrochemical performances of NCAT1 and NCAT2.

2.3. Role of Surface Structural Regulation

To understand the correlations between the regulated surface and the enhanced cycling stability, we investigated the surface structural and chemical evolution during the
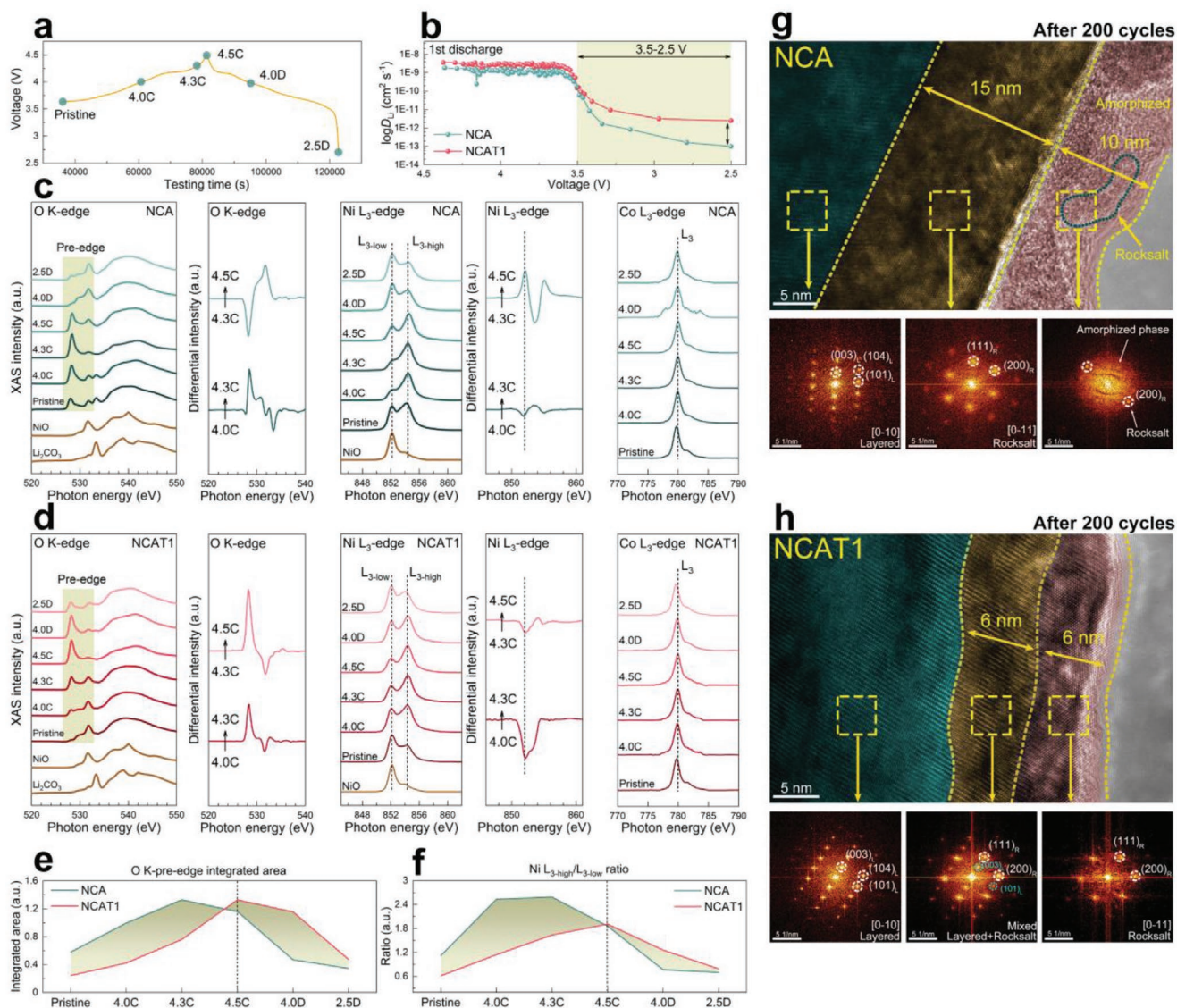
Figure 3. Regulated surface structure analyses: a) the designated points for the ex situ XAS testing during the first cycle at 0.1C rate between 2.5 and 4.5 V versus Li/Li+; b) The derived Li+ diffusion coefficient (D_{Li}) of NCA and NCAT1 during first discharging at 0.1C rate between 2.5 and 4.5 V based on the GITT data; c,d) Ex situ XAS spectra of normalized O K-edge, Ni L_3-edge, and Co L_3-edge of NCA and NCAT1 obtained at the designated points in a and the differential intensities of O K-edge and Ni L_3-edge between two designated points; e) O K-pre-edge integrated peak areas of NCA and NCAT1 at the designated points; f) Ni L_{3-high}/L_{3-low} ratios of NCA and NCAT1 at the designated points; g,h) HRTEM images of the fully discharged NCA and NCAT1 after 200 cycles and the corresponding FFT maps in the selected regions (L represents the layered phase, R represents the rock-salt phase).

charge–discharge process. We reveal that the Ta-rich regulated surface plays a critical role in enabling high reversibility of the lithiation/delithiation by preventing surface Ni reduction upon deep delithiation.

Previously, galvanostatic intermittent titration technique (GITT) were conducted for the first cycle of NCA and NCAT1 (Figure S8a, Supporting Information). The derived Li+ diffusion coefficient (D_{Li}) curves (Figure S8b: Supporting Information and **Figure 3**b) reveal that the average Li+ mobility of NCAT1 is higher than that of NCA. Note that the average D_{Li} of NCAT1 is almost one order of magnitude higher than that of NCA between 3.5 and 2.5 V, indicating a promoting kinetic of Li+ intercalation in NCAT1. In general, the sudden drop in Li+

mobility in the final stage of discharging can be attributed to the surface structural degradation and surface side reactions of materials.[20] In addition, the electrochemical impedance spectroscopy (EIS) results (Figure S9 and Table S8, Supporting Information) indicate that substantial impedance growth is observed in NCA, whereas slight growth is observed in NCAT1 after cycling. The XPS results (Figure S10, Supporting Information) indicate that fewer organic and inorganic impurities (e.g., RCO_xLi, $Li_xPO_yF_z$, and MF_2) formed on the surface of NCAT1 than on that of NCA after cycling, demonstrating that the continuous growth of the surface impedance is inhibited by the Ta-rich regulated surface. In addition, transition-metal ions dissolution testing (Figure S11, Supporting Information) shows

ADVANCED
SCIENCE NEWS
www.advancedsciencenews.com

NANO · MICRO
small
www.small-journal.com

that dissolved Ni and Co of NCA in electrolytes are higher than that of NCAT1 after storage at 85 °C for 5 days, and the gap is wider by the end of 10 and 15 days. These results demonstrate that the regulated surface structure is more stable, and prevents the unfavorable side reactions, thus suppressing transition-metal ions dissolution and the formation of the surface by-products during cycling. Hence, the origins of the improved discharge capacity and cycling stability are reasonably attributed to the stable surface structure and free Li^+ diffusion.

Considering the above evidence, a distinct surface structural and chemical evolution is expected for NCAT1 during lithiation/delithiation. To monitor these differences, ex situ XAS was conducted in the TEY mode during the first charge–discharge process. First, we assigned six points (Pristine, 4.0C, 4.3C, 4.5C, 4.0D, and 2.5D) corresponding to the pristine, 4.0 V charged, 4.3 V charged, 4.5 V charged, 4.0 V discharged, and 2.5 V discharged states, respectively, for ex situ XAS testing (Figure 3a). Figure 3c shows the normalized O K-edge, Ni L_3-edge, and Co L_3-edge of the XAS spectra for NCA, as well as the differential intensities of the O K-edge and Ni L_3-edge between two designated points. As shown in the O K-edge spectra of NCA, upon charging up to 4.3 V, the O K-pre-edge intensity increases and the Ni L_{3-low}-edge drops sharply, indicating the Ni^{3+} is oxidized to Ni^{4+} for providing charge compensation upon Li^+ extraction. However, upon charging from 4.3 to 4.5 V, the peak at 528 eV in the O K-edge associated with the $Ni^{3+/4+}$ 3d–O 2p antibonding level decreases and the peak at 532 eV assigned to the Ni^{2+} 3d–O 2p antibonding level increases, suggesting that $Ni^{3+/4+}$ ions partially reduce to Ni^{2+}. In addition, the differential intensity curves of the O K-edge of NCA clearly reveal the opposite trend of the intensity changes in the pre-edge region between the voltage ranges of 4.0–4.3 and 4.3–4.5 V. In addition, the differential intensity curves of the Ni L_3-edge prove that the oxidized $Ni^{3+/4+}$ ions of delithiated NCA partially reduce to Ni^{2+} upon deep delithiation, indicating that the surface Ni reduction can occur for NCA during first charging. In general, owing to the ionic radius of Ni^{2+} (0.69 Å) is close to that of Li^+ (0.76 Å), the reduced Ni^{2+} tends to migrate to the Li layer, hindering the Li^+ diffusion and triggering a continuous phase transition from original layered phase to final rock-salt phase.[21] Therefore, the reduction of oxidized $Ni^{3+/4+}$ induces a large impedance buildup, as presented in the EIS and XPS results, and is detrimental to the electrochemical properties.

Regarding the O K-edge spectra of NCAT1 in Figure 3d, the continuous growth of the pre-edge intensity indicates that Ni is continuously oxidized upon charging until 4.5 V. The Ni L_3-edge spectra also show the stable growth of the Ni oxidation states. In addition, the differential intensity curves of the O K-edge and Ni L_3-edge clearly outline a steadily increasing trend of the Ni oxidation states upon charging. These results reveal that the Ta-rich regulated surface of NCAT1 reduces the chemically unstable Ni^{4+} ions and prevents the surface Ni reduction in deep delithiation, enabling highly reversible Li^+ insertion/extraction, which thus exhibits an improved Li^+ mobility during discharging, as displayed in Figure 3b. Furthermore, the O K-pre-edge integrated peak areas of the assigned points of NCAT1 are smaller than that of NCA during charging (Figure 3e), indicating that the Ta substitution decreases and maintains a low level of the TM-O covalency (mainly Ni-O)
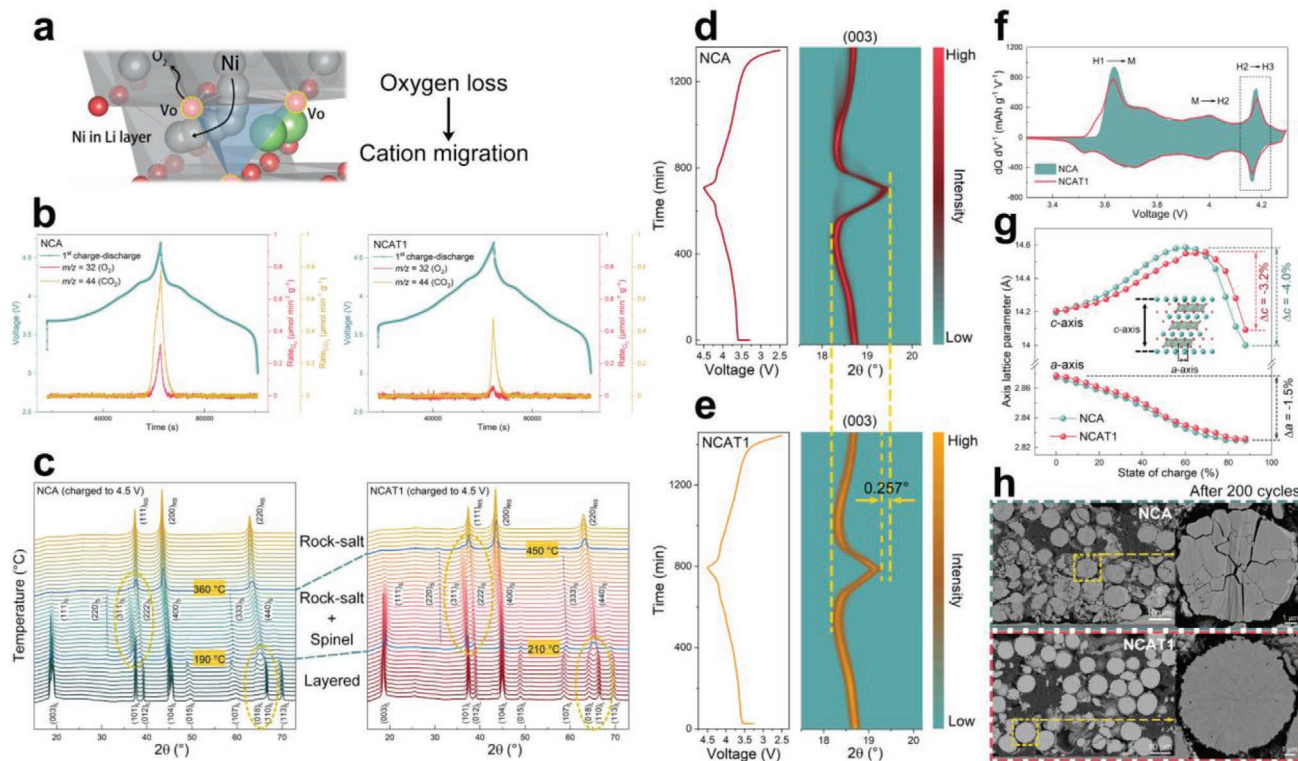
upon Li^+ extraction; this may causes less TM 3d-O 2p orbital hybridization and fewer electrons depletion in the occupied O 2p orbitals, thus contributing to suppress oxygen loss. In addition, the Ni L_{3-high}/L_{3-low} ratio variations in Figure 3f further confirm that the continuous increasing trend of Ni oxidation states of NCAT1 and the Ni reduction of NCA during 4.3–4.5 V. The peak positions in the Co L_3-edge XAS spectra of NCA and NCAT1 display negligible variations, suggesting that $Co^{3+/4+}$ (the redox couple in $LiCoO_2$) would not be triggered to participate in charge compensation.

To evaluate the effects of the surface structural regulation, the notable differences of the surface structures for NCA and NCAT1 after 200 cycles were observed in the HRTEM images, as shown in Figure 3g,h. The NCA cathode after 200 cycles exhibits a three-layer surface structure, as denoted by the dashed yellow lines. The outermost layer (≈10 nm) is composed of an amorphized rock-salt structure, as indexed by the dispersed halo and the diffraction spots in its counterpart FFT map, which results from the undesirable side reactions.[22] A clear rock-salt phase of ≈15 nm underneath the amorphized layer is identified by the corresponding FFT map. The original layered phase lies nearly 25 nm below the surface. These features reveal the severe surface degradation of NCA. However, the NCAT1 cathode after 200 cycles exhibits well-ordered surface structures without an amorphized phase, which is constructed by a well-defined rock-salt phase (the outermost layer, ≈6 nm) and a mixed phase (the middle layer, ≈6 nm). Such a stabilized surface illustrates that the regulated surface inhibits undesirable structural transitions and side reactions, maintaining high Li^+ mobility on the surface during cycling.

Overall, the Ta-rich regulated surface structure has optimal structural and chemical stability; this is because the Ta substitution on the surface decrease the amount of the highly active $Ni^{3+/4+}$, and it also prevents the surface Ni reduction in deep charging, presenting a steady upswing trend of Ni oxidation states, which thus suppresses surface structural deterioration and undesirable side reactions. Such a surface structural regulation is a significant reason for the higher Li^+ mobility of NCAT1 than that of NCA during discharging. Therefore, NCAT1 with a stable regulated surface exhibits enhanced rate capability, Coulombic efficiency, and cycling stability.

2.4. Effects on Bulk Structural Stability and Integrity

As discussed above, a high degree of Ni reduction in deep delithiation is an important reason for inducing structural collapse because Ni^{2+} is more easier to migrate to the Li Layer than $Ni^{3+/4+}$. Besides, lattice oxygen loss, a significant source of structural degradation, decreases the migration energy barrier and thus allows for easily cation migrating to the Li layer, also deserving attention, as displayed in **Figure 4**a.[23] Lattice oxygen loss not only is a surface-level issue, but also involves bulk structure. The accumulation of the subsurface and bulk lattice oxygen vacancy ultimately leads to the O_2 release from the material surface, which further oxidizes electrolyte solvents and generates heat, resulting in unfavorable structural deterioration of materials and safety risks of batteries.[24] In this section, we revel that Ta substitution stabilizes integrated

ADVANCED
SCIENCE NEWS
www.advancedsciencenews.com

NANO · MICRO
small
www.small-journal.com

Figure 4. Effects on bulk structural stability and integrity: a) Schematic of the correlation of oxygen loss and cation migration; b) O_2 and CO_2 evolution rates during in-situ DEMS measurements and the corresponding voltage profiles of NCA and NCAT1 cycled at 0.1C between 3.0 and 4.7 V; c) In situ heating XRD profiles of NCA and NCAT1 charged to 4.5 V between 25 and 500 °C; d,e) In situ XRD contour maps and the corresponding voltage profiles of NCA and NCAT1 during the first cycle between 2.5 and 4.5 V. f) dQ dV^{-1} curves of NCA and NCAT1 between 2.5 and 4.3 V; g) Variations of the derived a-axis and c-axis lattice parameters as a function of the state of charge from the in-situ XRD data. Insets: schematic diagram of the a-axis and c-axis lattice parameters of typical layered oxides ($R\bar{3}m$); h) Cross-sectional SEM images of NCA and NCAT1 electrodes after 200 cycles.

oxygen-skeleton stability and suppresses the oxygen loss, thus improving the bulk structural and thermal stability. In addition, Ta substitution restricts the severe lattice shrinkage during cycling, improving the bulk structural integrity that avoids the failure of the regulated surface.

First, by conducting in situ DEMS measurements (Figure 4b), we note that, compared with NCA, the O_2 release rate is remarkably reduced in NCAT1, illustrating that the Ta substitution suppresses the oxygen loss. To further evaluate the integrated structural stability, in situ heating XRD measurements were conducted to explore the structural evolution during the heating process of the charged cathodes. As shown in Figure 4c, both NCA and NCAT1 sequentially undergo crystal structural changes from the layered phase to the spinel phase and subsequently to the rock-salt phase with increasing temperature. NCAT1 displays a delayed transformation temperature of 210 °C from the layered phase to the spinel phase compared with NCA (190 °C). More remarkably, the transformation temperature from the spinel to rock-salt phase leaps to 450 °C for NCAT1, whereas it is only 360 °C for NCA. This result illustrates that the stable bulk structure associated with oxygen skeleton of NCAT1 enhances its thermal stability. Further, the differential scanning calorimeter (DSC) measurements (Figure S14, Supporting Information) show a delayed exothermic peak and decreased exothermic quantity for NCAT1 compared with that for NCA. These findings are in accordance

with the thermogravimetric (TG) test results (Figure S15, Supporting Information), indicating that Ta substitution can significantly suppresses the lattice oxygen loss and coupled cation migration, improving the thermal stability of cathodes. The fundamental reason of the oxygen-skeleton stabilization is the charge regulation that will discussed in detail in Section 2.5.

Regarding another significant effect of Ta substitution on bulk structure, we confirm that Ta substitution suppresses the microcracks of secondary particles, preventing fresh surfaces from being exposed to electrolytes. To establish the relationships between integrated structural properties and electrochemical behaviors, in situ XRD measurements were conducted during the charge–discharge process (Figure 4d,e). The shift of the (003) peak position of NCA to a high degree at ≈4.2 V shows that a dramatic lattice contraction occurs along the c-axis. Meanwhile, the redox peaks corresponding the H2–H3 phase transition emerge, as shown in Figure 4f, suggesting that the H2–H3 phase transition is accompanied by the severe lattice contraction. However, the (003) peak of NCAT1 is less shifted, with an angle difference of 0.257° compared to NCA, indicating that the lattice contraction along the c-direction is mitigated by Ta substitution, thus presenting a suppressed peak intensity corresponding the H2–H3 phase transition for NCAT1 (more detailed diffraction peak evolution information in the in situ XRD counter maps is displayed in Figures S12 and S13: Supporting Information). The refined c-axis and a-axis lattice

ADVANCED
SCIENCE NEWS
www.advancedsciencenews.com

NANO · MICRO
small
www.small-journal.com

parameters from the in situ XRD data obtained using the Rietveld method (Figure 4g) confirm that the maximum contraction extent of the c-axis (Δc) of NCA is 4.0%, whereas that of NCAT1 is 3.2%. The unit-cell contraction along the a-axis ($\Delta a = 1.5\%$) is nearly identical for both NCA and NCAT1, illustrating that the volume shrinkage of the unit cell is highly anisotropic. Such severe anisotropic lattice expansion and shrinkage of NCA during lithiation/delithiation causes the accumulation of local stress and breaks the integrity of the secondary particles, leading to the generation and propagation of microcracks. As shown in Figure 4h, the cross-sectional SEM images of the NCA electrode after 200 cycles present substantial intergranular cracks, exposing fresh surfaces for the uninterrupted solid–liquid side reactions, and thus leading to continuous impedance buildup.[25] Surprisingly, these cracking barely occur in the NCAT1 electrode, revealing that the anisotropic lattice shrinkage are restricted by Ta substitution, thus preventing the formation of microcracks and associated degradation route. Further, the complete grains and particles of NCAT1 ensure the availability of the regulated surface for long-term cycling.

In short, by monitoring the surface and bulk structural evolution and gas release upon lithiation/delithiation and heating, we determined that Ta substitution suppresses the oxygen loss and associated bulk structural degradation. Besides, the limited lattice distortion induced by Ta substitution prevents the formation of microcracks, which thereby inhibits the fragmentation of secondary particles during long-term cycling. In addition, the stable oxygen skeleton of NCAT1 provides remarkable thermal stability, as presented in the above analyses.

2.5. Role of Charge Regulation

Considering that Ta substitution suppresses lattice shrinkage and oxygen loss during cycling as evidenced in Section 2.4, more in-depth mechanisms are required to elucidate the origins of such structural integrity and stability. In this section, the density functional theory (DFT) calculations reveal that the suppressed lattice shrinkage originates from the boosted oxygen charge and its localization. In addition, such a localized oxygen charge weakens the hybridization degree between Ni and O electrons, leading to the depopulation of O 2p electrons in TM 3d–O 2p antibonding orbitals, which could be responsible for the suppressed oxygen loss and oxygen-skeleton stabilization.

First, a simplified $4 \times 4 \times 1$ supercell including 192 atoms for NCA ($Li_{48}Ni_{48}O_{96}$) and NCAT ($Li_{48}Ni_{47}Ta_1O_{96}$) was constructed as a convenient means of probing the effects of Ta on the bulk structure. To understand the electronic charge regulation intuitively, 2D charge density slice for NCAT (**Figure 5**a) shows that substantial electrons are depleted at the Ta sites. This is because the highly ionized Ta^{5+}, which acts as an electron donor, provides extra electrons to disperse outward to balance the charge neutrality of the system. In addition, electron localization occurs among Ta and the neighboring Ni and O in NCAT, indicating less covalency for the Ta–O bonds and the neighboring Ni–O bonds in NCAT than those in NCA. This result can also be verified by the decreased O K-pre-edge integrated peak area of NCAT1, as shown in the abovementioned XAS and EELS analyses. Further, the Bader charge analysis

results (Table S9, Supporting Information) provided the quantitative data for the evaluation of the charge redistribution, revealing that the nearest neighboring Ni (first Ni-shell) and O (first O-shell) around the Ta site gain more electrons in NCAT than in NCA. The increased net charges (the number of electrons transferred) of O and Ni in NCAT confirm the charge regulation around the Ta site—an increase in the neighboring Ni and O partial charge. In addition, the average oxygen vacancy formation energy for the first O-shell of Ta in NCAT (0.84 eV) is much larger than that in NCA (0.32 eV), illustrating the improved oxygen stability for NCAT that is associated with the improved oxygen partial charge.

To further probe the charge distribution variation during delithiation, electronic localization function (ELF) analysis was conducted for NCA and NCAT ($x_{(Li)} = 1$, 0 in Li_xTMO_2). As shown in Figure 5d, the ELF contour map of the pristine NCA shows separated localized electrons, which are identified as the core electrons of Ni and O and the nonbonding t_{2g} electrons of the Ni–O bonds. When Li ions are fully extracted in NCA, the localized electron regions of Ni and O become much larger and combined, becoming indistinguishable. This phenomenon indicates that the degree of electronic delocalization increases sharply after Li extraction, i.e., Ni–O bonds become more covalent. However, the localized electron regions in NCAT retain stable shapes and exhibit clear separation even in the fully delithiated state. Such strong electron localization of O charge in NCAT indicates that Ta decreases the Ni–O covalency in the local environments and maintains its covalency at a low level during Li^+ extraction.

Based on the above analysis, the stabilization mechanism associated with the restricted lattice shrinkage of NCAT can be clarified, as illustrated in Figure 5g. Upon Li^+ extraction, the "screening effect" of Li ions decreases gradually, and thus the upper and lower O layers are immediately opposite to each other, increasing the interlayer electrostatic repulsion and interlayer spacing.[26] However, the Ni–O bonds become more covalent and the electron hybridization between Ni and O become stronger, due to the continuous oxidation of Ni, reducing the partial charge on O, weakening the electrostatic repulsion between the O layers, and causing severe lattice shrinkage in deep delithiation. Hence, there are two obviously competing interactions—the increased electrostatic repulsion between the O layers induced by Li^+ extraction and the decreased O partial charge induced by the enhanced Ni–O covalency—result in an increase and subsequent decrease of the c-axis lattice parameter upon delithiation, that is, the severe lattice shrinkage in deep charging is originated from strong Ni–O covalency.

However, the charge regulation induced by Ta substitution boosts the O charge, and prevents the delocalization of O charge in deep delithiation with weakened TM–O covalent bonds, reinforcing the interlayer repulsion, and thus suppressing the severe lattice shrinkage along the c-axis upon deep charging. For these reasons, the associated microcracks are relieved, enabling the structural integrity, as displayed in Figure 4h.

By monitoring the calculated net charges of O and magnetic moments of Ni in NCA and NCAT with different delithiation states, the anionic redox emerges. Typical delithiated configurations of the Li_xNiO_2 were adopted, as displayed in Figure S16 (Supporting Information). In light of the different electronic
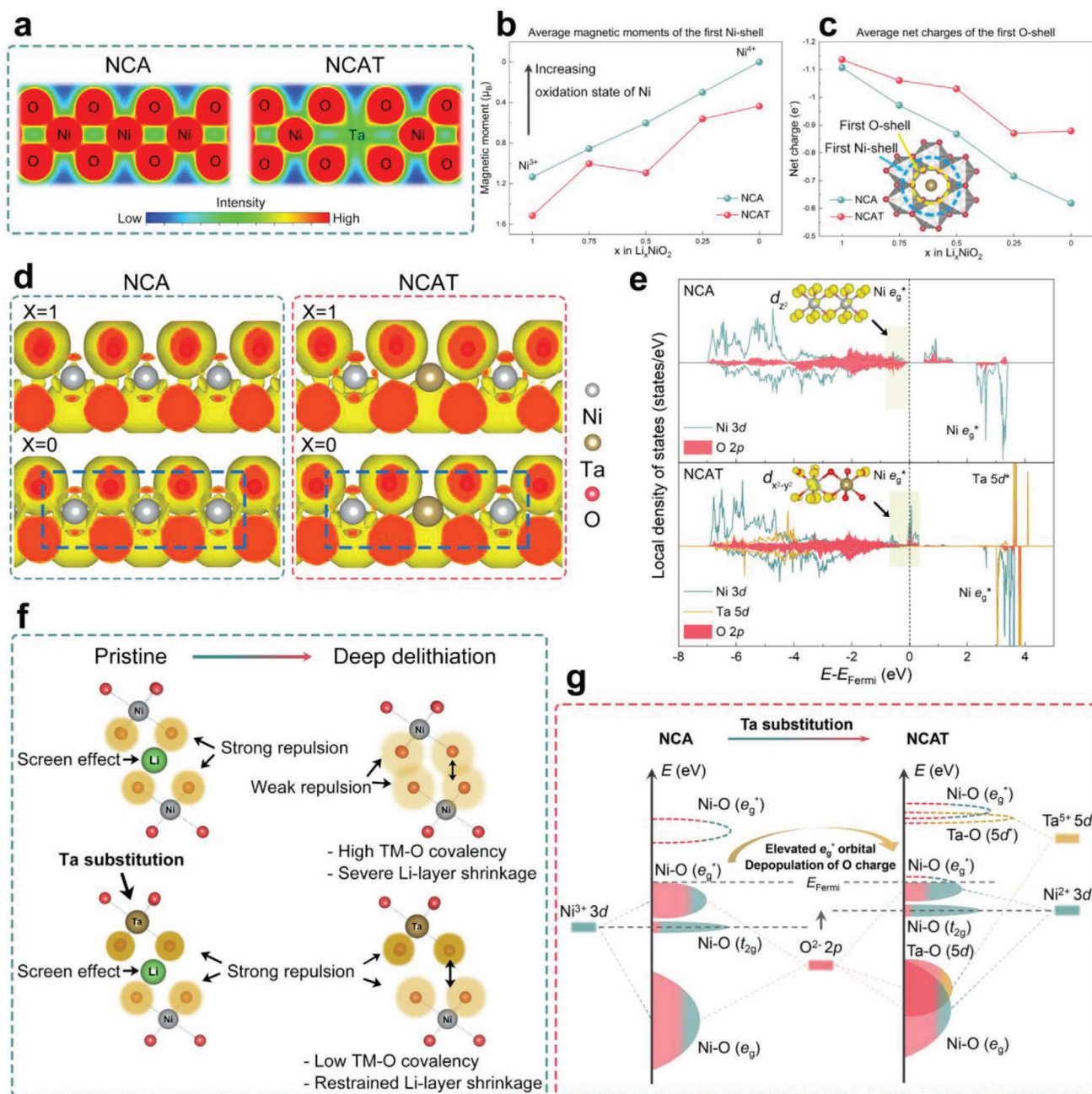
Figure 5. DFT calculations for Li-Ni-Ta-O system: a) 2D contour maps of charge density distribution of NCA and NCAT (isosurface level = 0.1 e Bohr^{-3}, (−114) lattice plane); b,c) Average magnetic moments of the first Ni-shell and average net charges of the first O-shell for NCA and NCAT as a function of Li concentration ($x = 1$, 0.75, 0.5, 0.25, 0 in Li$_x$TMO$_2$); Inset: schematic of the first Ni-shell and the first O-shell in NCAT; d) ELF analysis of NCA and NCAT at pristine and fully charged state ($x = 1$, 0 in Li$_x$TMO$_2$) with an isosurface level of 0.084 e Bohr^{-3}; e) LDOS of Ni 3d, O 2p in NCA and Ta 5d, the neighboring Ni 3d, and O 2p in NCAT (Fermi level is set at 0 eV); Insets: calculated partial charge density distribution of the valence band maximum near the Fermi level for NCA and NCAT1; f) Schematic of the charge regulation mechanism; g) Schematic of the energy band structural regulation.

filling between Ni^{3+} ($t_{2g}^6 e_g^1$) and Ni^{4+} ($t_{2g}^6 e_g^0$), in absolute terms, the average magnetic moment of Ni in NCA (Figure 5b) gradually decreases from 1.14 to 0 μ_B upon delithiation, indicating that the oxidation state of Ni increases from 3+ to 4+ for charge compensation. Simultaneously, the average net charge of O in NCA (Figure 5c) continuously increases from −1.10 e$^-$ to −0.62 e$^-$, illustrating that the O electrons also loses as Li$^+$ extraction. These results directly reveal the unfavorable O oxidation.

In general, O is considered as a beholder and plays a role of structural skeleton for free Li$^+$ diffusion and TM redox during Li$^+$ insertion/extraction in the conventional layered cathodes (Li$_x$TMO$_2$, $x \leq 1$), because the TM redox couples (e.g., Ni$^{2+/3+/4+}$, Co$^{3+/4+}$) are pinned on the top of the O 2p band.[13] However, the increased average net charge of O and large amounts of O$_2$ release in the DEMS measurements suggest that the lattice oxygen are unstable and can be oxidized; this kind of oxygen

charge oxidation is originated from the charge delocalization nature of the layered cathodes in deep delithiation. While charge compensation during delithiation is provided by TM redox, substantial delocalized electrons around O would inevitably be partially removed through the highly covalent $Ni^{3+/4+}$–O bonds, generating oxygen defects and/or oxygen vacancies, thus triggering continuous cation migration and structural collapse. In contrast, the net charges of O around the Ta in NCAT remain relatively steady upon delithiation, confirming that the O charge in NCAT are less likely to delocalization and loss, as evidenced by the variation of the O K-pre-edge peak areas in Figure 3e.

Furthermore, the oxygen charge localization is bound to tune the TM-O bonding interactions, thus affecting the band structure of the system. As shown in Figure 5e, the local density of states (LDOS) was calculated to explore the band structure variations. The LDOS of Ni 3d and O 2p in NCA clearly show a low-spin Ni^{3+} orbital feature assigned to the electronic configuration of $t_{2g}^{6}e_{g}^{1}$ and a large orbital overlap between the Ni 3d and O 2p electrons. In contrast, the LDOS of Ni 3d, Ta 5d, and O 2p in NCAT display different characteristics, in which a half-filled impurity band can be assigned to the e_{g}^{*} antibonding orbitals of Ni across the Fermi level. Such bands are induced by Ta substitution with the injection of extra electrons into the neighboring Ni and O, thus changing the orbital occupation of Ni, which are confirmed by the calculated partial charge density distribution. As shown in the insets, the electrons in the valence band maximum of NCAT are localized in the e_{g}^{*} orbital d_{x2-y2} with a higher crystal field level, forming Ni^{2+}, whereas that of NCA is localized in the e_{g}^{*} orbital d_{z2} assigned to Ni^{3+}. This finding demonstrates that Ta changes the occupation states of the e_{g}^{*} antibonding orbitals of the neighboring Ni, presenting a formal oxidation state change of the neighboring Ni from 3+ to 2+ and the elevation of the e_{g}^{*} level of Ni 3d. The calculated d-band center also confirms the elevated energy level of Ni 3d band with respect to the Fermi level, as listed in Table S10 (Supporting Information). In addition, the occupied e_{g}^{*} orbitals of NCAT shows reduced overlap between the Ni 3d and O 2p electrons, and most of the O 2p electrons shift to lower energies, indicating that the population of O 2p electrons in the e_{g}^{*} orbitals is reduced. For the LDOS of Ta 5d, the bonding orbitals are all occupied and the antibonding orbitals are all empty, demonstrating high chemical stability and electrochemically inactive state of Ta^{5+} as its $5d^0$ configuration.

Figure 5g provides a schematic of band structural regulation associated with the occupied energy level of electrons. As the free-atom level of neighboring Ni 3d that obtains extra electrons, induced by Ta substitution, shifts to a higher energy, the corresponding molecular Ni 3d–O 2p hybridized e_g and e_g^{*} orbitals are also shifted to higher energies. The higher energy of the e_g^{*} level becomes more far away from the O 2p atomic level, and thus, the population weight of the e_g^{*} orbitals shifts toward the Ni 3d electrons and the contribution of O 2p electrons to the e_g^{*} orbitals decreases accordingly. Owing to the negative feedback regulation, the decreasing population of O 2p electrons in the e_g^{*} orbitals induce an increasing population of O 2p electrons in the e_g orbitals to balance the net local charge fluctuation.[27] Thus, such less contribution of O charge to the antibonding level (frontier orbitals) causes less participation

in the redox reactions and undesirable oxygen oxidation, suppressing the oxygen defects and associated oxygen loss.

Based on the above charge distribution and band structure analyses, the charge regulation induced by Ta substitution occurs between the dopants and host ions via charge transfer, as well as in the band structure via the changed TM–O bonding interactions. Ultimately, the increased oxygen charge strengthens the interlayer repulsion in deep delithiation, suppresses microcracks, and thus improves the structural integrity, which in turn prevents the fragmentation of the regulated surface after long-term cycling. Besides, the depopulation of oxygen charge in the TM 3d-O 2p antibonding level suppresses the undesirable oxygen oxidation, and improves the oxygen-skeleton stability, thus improving the structural and thermal stability.

3. Conclusion

In summary, this study presents an integrated picture of the functional mechanisms of high-valence Ta^{5+} substitution in Ni-rich cathodes and elucidates the critical role of surface structure and bulk charge regulation in dominating the promotion of the electrochemical properties.

Specifically, the regulated surface structure induced by partial Ta enrichment suppresses surface Ni reduction in deep charging, preventing undesirable side reactions and structural collapse, and thus providing a stable framework for reversible Li^+ insertion/extraction. Moreover, charge regulation occurs after introducing Ta in the bulk, boosting oxygen charge and its localization. Such an enhanced localized oxygen charge resists the intrinsic O charge delocalization of Ni-rich layered oxides during Li^+ extraction, mitigating the severe lattice shrinkage and associated microcracks, and thus preventing the fragmentation of the regulated surface after long-term cycling. In addition, O charge localization regulates the band structure of the system, resulting in a depopulation of O charge in the TM 3d–O 2p antibonding level, thus suppressing the undesirable oxygen oxidation and loss, and further stabilizing the bulk structure.

By integrating these effects, both surface and bulk structures are stabilized to achieve the superior electrochemical properties and thermal stability. The well-designed NCAT2 cathode exhibits a remarkable capacity retention of 80% up to 768 cycles with a high initial discharge capacity of 183.1 mAh g^{-1} at 1C rate versus Li/Li^+. This study emphasizes the significance of the surface structure and bulk charge distribution for Ni-rich cathodes in improving electrochemical properties and provides a promising integrated optimization strategy for Ni-rich cathodes. These findings are expected to provide guidelines for the rational design of stable and reliable Ni-rich cathodes.

4. Experimental Section

Materials Synthesis: The pristine $LiNi_{0.88}Co_{0.10}Al_{0.02}O_2$ materials were prepared by mixing commercial precursor $Ni_{0.88}Co_{0.10}Al_{0.02}(OH)_2$ (Kelong Group) with lithium source $LiOH·H_2O$ (Aladdin, 99.9%) (1 mol% excess). Then the mixture was heated at 480 °C for 5 h and 730 °C for 12 h at 3 °C min^{-1} under O_2 flow. As the $LiNi_{0.88}Co_{0.10}Al_{0.02}Ta_xO_2$ materials ($x = 0.004$ or 0.008), 0.2 mol precursor was dispersed into 200 mL

anhydrous ethanol, followed by adding stoichiometric tantalum ethoxide ($C_{10}H_{25}O_5Ta$, Aladdin, 99.99%). The suspension solution was slowly evaporated at 80 °C with continuous stirring until desiccation, and then dried overnight at 100 °C. Later, the collected powder was mixed with an excess of 1 mol% $LiOH·H_2O$ and subsequently calcinated under the same condition as that of the pristine sample to obtain the final product.

Materials Characterization: The element compositions of NCA, NCAT1, and NCAT2 samples and the content of dissolved Ni and Co in electrolytes of NCA and NCAT1 were determined by ICP-OES (PerkinElmer Optima 8300). The XRD was conducted using a parallel beam XRD instrument (Smartlab, Rigaku) with Cu Kα radiation (λ = 1.5406 Å) in the scan range (2θ) of 10–120°. The in situ electrochemical XRD spectra were continuously recorded from 15–80° during the first cycling at a current rate of 0.1C between 2.5 and 4.5 V. The XRD profiles were refined by Rietveld refinement methods using the GSAS software with the EXPGUI interface.[28] The in situ heating XRD measurements of the charged cathodes (4.5 V) were performed during heating by stage from 25 to 500 °C, with a heating rate of 3 °C min^{-1}. The surface and cross-section images of the samples were observed by a field-emission scanning electron microscope (SEM, JSM-7900F, JEOL) and the cross-section samples were operated using a cross-sectional polisher (IB-19520CCP, JEOL). The microstructure of the materials were obtained from a high resolution transmission electron microscopy (HRTEM, Tecnai G^2 F20) and an AC-TEM equipped with double Cs correctors (JEM-ARM200F). The cross-sectional line scanning of NCAT1 was conducted by electron probe micro-analyzer (EPMA, JXA 8230) and STEM-EDS measurements. The focused ion beam (FIB, Thermo Scientific Scios 2) was used to prepare the samples for AC-TEM measurements. The surface element analyses were performed by XPS (Thermo Fisher ESCALAB 250Xi) and all data were corrected by C 1s peak at 284.8 eV. The DSC measurements of the charged electrodes (4.5 V) were performed on Mettler DSC 3 at a heating rate of 3 °C min^{-1} from 25 to 500 °C. The TG analysis of the delithiated powder was carried out using a Mettler TGA/DSC analyzer (TGA/DSC 3+) at a heating rate of 3 °C min^{-1} between 25 and 500 °C under N_2 flow. The synchrotron XAS of O K-edge and Ni/Co L-edges were measured on the beamline MCD (BL12B) at Nation Synchrotron Radiation Laboratory (NSRL, Hefei) in TEY mode by collecting the drain current under a vacuum better than 1×10^{-7} Pa. The energy resolution is ≈0.2 eV with an energy range from 100 to 1000 eV. For in situ gas evolution analysis, the DEMS measurements were conducted on i-DEMS 100 (Linglu Instruments Co., Lt, Shanghai) with a constant carrier gas flow (Argon, 0.7 mL min^{-1}).

Electrochemical Measurements: Standard 2032 coin-type half-cells were fabricated by using a Li metal as the anode, Celgard 2400 separator and a 1 M $LiPF_6$ in a mixture of diethyl carbonate (DEC), dimethyl carbonate (DMC), and ethylene carbonate (EC) (volume ratio of 1:1:1) as the electrolyte in an Argon-filled glove box. Cathodes were fabricated by mixing active materials, carbon black (Super-P) and polyvinylidene fluoride (PVDF) binder (weight ratio of 8:1:1) in *N*-methyl pyrrolidinone (NMP). The obtained slurry was coated on Al foil and then dried at 80 °C for 4 h with a mass of the loaded active materials of ≈5.5 mg cm^{-2}. Long-term cycling measurements were conducted in a pouch-type full cell. The cathode active materials were mixed with PVDF and Super-P with a weight ratio of 97:2:1 in NMP to form a slurry coated on Al foil. The graphite as anode, coated in a 94:2:4 weight ratio with Super-P and carboxymethyl cellulose (CMC) binder on Cu foil, were used. The active materials loading level of the cathode was ≈22 mg cm^{-2} and the loading level of graphite of the anode was ≈14 mg cm^{-2}. The same electrolyte used in the half-cell testing was employed in the full-cell. The N/P ratio was fixed at ≈1.10. The full-cells were charged to 3.7 V in the first charging process to eliminate the generated gas (degassing process). A three-formation cycle was performed at 0.1 C before long-term cycling. The full cells were charged and discharged between 2.8 and 4.2 V at a rate of 1 C at 25 °C versus graphite under CC–CV mode (constant current at 1C rate and constant voltage at 4.2 V with a cut-off current of 0.05C). Electrochemical tests were conducted on a battery tester (LAND CT2001A) in galvanostatic mode. For the GITT measurements, the half-cells were charged and discharged by stage in galvanostatic mode

at 0.1C with constant current for 600 s followed with 2400 s relaxation between 2.5 and 4.5 V at 25 °C. The EIS testing of the charged cells (4.3 V) were conducted using an electrochemical workstation (Autolab) in a frequency range from 100 kHz to 0.01 Hz with a perturbation amplitude of ±10 mV at 25 °C.

First-principles calculations are illustrated in detail in the Supporting Information.

Supporting Information

Supporting Information is available from the Wiley Online Library or from the author.

Conflict of Interest

The authors declare no conflict of interest.

Data Availability Statement

Research data are not shared.

[1] F. Wu, J. Maier, Y. Yu, *Chem. Soc. Rev.* **2020**, *49*, 1569.

[2] W. Li, E. M. Erickson, A. Manthiram, *Nat. Energy* **2020**, *5*, 26.

[3] a) C. Xu, K. Marker, J. Lee, A. Mahadevegowda, P. J. Reeves, S. J. Day, M. F. Groh, S. P. Emge, C. Ducati, B. Layla Mehdi, C. C. Tang, C. P. Grey, *Nat. Mater.* **2021**, *20*, 84; b) S. Li, Z. Jiang, J. Han, Z. Xu, C. Wang, H. Huang, C. Yu, S. J. Lee, P. Pianetta, H. Ohldag, J. Qiu, J. S. Lee, F. Lin, K. Zhao, Y. Liu, *Nat. Commun.* **2020**, *11*, 4433.

[4] S. H. Song, M. Cho, I. Park, J. G. Yoo, K. T. Ko, J. Hong, J. Kim, S. K. Jung, M. Avdeev, S. Ji, S. Lee, J. Bang, H. Kim, *Adv. Energy Mater.* **2020**, *10*, 2000521.

[5] Q. Lin, W. Guan, J. Meng, W. Huang, X. Wei, Y. Zeng, J. Li, Z. Zhang, *Nano Energy* **2018**, *54*, 313.

[6] a) J. R. Croy, D. C. O'Hanlon, S. Sharifi-Asl, M. Murphy, A. Mane, C.-W. Lee, S. E. Trask, R. Shahbazian-Yassar, M. Balasubramanian, *Chem. Mater.* **2019**, *31*, 3891; b) K. Min, K. Park, S. Y. Park, S.-W. Seo, B. Choi, E. Cho, *J. Electrochem. Soc.* **2018**, *165*, A79; c) P. Yan, J. Zheng, J. Liu, B. Wang, X. Cheng, Y. Zhang, X. Sun, C. Wang, J.-G. Zhang, *Nat. Energy* **2018**, *3*, 600.

[7] G. Li, Z. Huang, Z. Zuo, Z. Zhang, H. Zhou, *J. Power Sources* **2015**, *281*, 69.

[8] a) Y. Bi, J. Tao, Y. Wu, L. Li, Y. Xu, E. Hu, B. Wu, J. Hu, C. Wang, J.-G. Zhang, *Science* **2020**, *370*, 1313; b) G. W. Nam, N.-Y. Park, K.-J. Park, J. Yang, J. Liu, C. S. Yoon, Y.-K. Sun, *ACS Energy Lett.* **2019**, *4*, 2995.

[9] T. He, L. Chen, Y. Su, Y. Lu, L. Bao, G. Chen, Q. Zhang, S. Chen, F. Wu, *J. Power Sources* **2019**, *441*, 227195.

[10] H.-H. Ryu, N.-Y. Park, T.-C. Noh, G.-C. Kang, F. Maglia, S.-J. Kim, C. S. Yoon, Y.-K. Sun, *ACS Energy Lett.* **2021**, *6*, 216.

[11] L. de Biasi, A. Schiele, M. Roca-Ayats, G. Garcia, T. Brezesinski, P. Hartmann, J. Janek, *ChemSusChem* **2019**, *12*, 2240.

[12] S. Sharifi-Asl, J. Lu, K. Amine, R. Shahbazian-Yassar, *Adv. Energy Mater.* **2019**, *9*, 1900551.

[13] A. Grimaud, W. T. Hong, Y. Shao-Horn, J. M. Tarascon, *Nat. Mater.* **2016**, *15*, 121.

[14] a) W. Lee, S. Yun, H. Li, J. Kim, H. Lee, K. Kwon, J. Y. Lee, Y. M. Choi, W. S. Yoon, *Small* **2020**, *16*, 1905875; b) Z. W. Lebens-Higgins, N. V. Faenza, M. D. Radin, H. Liu, S. Sallis, J. Rana, J. Vinckeviciute, P. J. Reeves, M. J. Zuba, F. Badway, N. Pereira, K. W. Chapman, T.-L. Lee, T. Wu, C. P. Grey, B. C. Melot, A. Van Der Ven, G. G. Amatucci, W. Yang, L. F. J. Piper, *Mater. Horiz.* **2019**, *6*, 2112.

[15] J. Li, R. Doig, J. Camardese, K. Plucknett, J. R. Dahn, *Chem. Mater.* **2015**, *27*, 7765.

[16] F. Lin, D. Nordlund, I. M. Markus, T.-C. Weng, H. L. Xin, M. M. Doeff, *Energy Environ. Sci.* **2014**, *7*, 3077.

[17] E. Hu, X. Wang, X. Yu, X. Q. Yang, *Acc. Chem. Res.* **2018**, *51*, 290.

[18] S. Liu, Z. Liu, X. Shen, X. Wang, S. C. Liao, R. Yu, Z. Wang, Z. Hu, C. T. Chen, X. Yu, X. Yang, L. Chen, *Adv. Energy Mater.* **2019**, *9*, 1901530.

[19] G. Ceder, Y.-M. Chiang, D. Sadoway, M. Aydinol, Y.-I. Jang, B. Huang, *Nature* **1998**, *392*, 694.

[20] Y. Lyu, N. Zhao, E. Hu, R. Xiao, X. Yu, L. Gu, X.-Q. Yang, H. Li, *Chem. Mater.* **2015**, *27*, 5238.

[21] S. H. Song, M. Cho, I. Park, J. G. Yoo, K. T. Ko, J. Hong, J. Kim, S. K. Jung, M. Avdeev, S. Ji, *Adv. Energy Mater.* **2020**, *10*, 2000521.

[22] H. Zhang, B. M. May, F. Omenya, M. S. Whittingham, J. Cabana, G. Zhou, *Chem. Mater.* **2019**, *31*, 7790.

[23] S. S. Zhang, *Energy Storage Mater.* **2020**, *24*, 247.

[24] F. Kong, C. Liang, L. Wang, Y. Zheng, S. Perananthan, R. C. Longo, J. P. Ferraris, M. Kim, K. Cho, *Adv. Energy Mater.* **2019**, *9*, 1802586.

[25] K.-J. Park, H.-G. Jung, L.-Y. Kuo, P. Kaghazchi, C. S. Yoon, Y.-K. Sun, *Adv. Energy Mater.* **2018**, *8*, 1801202.

[26] J. Tarascon, G. Vaughan, Y. Chabre, L. Seguin, M. Anne, P. Strobel, G. Amatucci, *J. Solid State Chem.* **1999**, *147*, 410.

[27] H. Raebiger, S. Lany, A. Zunger, *Nature* **2008**, *453*, 763.

[28] a) B. H. Toby, *J. Appl. Crystallogr.* **2001**, *34*, 210; b) A. Larson, R. Von Dreele, *Los Alamos, New Mexico: Los Alamos National Laboratory* **2004**.